Earth and Planetary Science Letters 584 (2022) 117506

Contents lists available at ScienceDirect

Earth and Planetary Science Letters

www.elsevier.com/locate/epsl

On the origin of the Canary Islands: Insights from mantle convection modelling

Ana M. Negredo [a,b,*], Jeroen van Hunen [c], Juan Rodríguez-González [c], Javier Fullea [a]

[a] Departamento de Física de la Tierra y Astrofísica, Facultad de CC. Físicas, Universidad Complutense de Madrid, Plaza de Ciencias 1, 28040 Madrid, Spain
[b] Instituto de Geociencias IGEO (CSIC, UCM), Madrid, Spain
[c] Department of Earth Sciences, Durham University, Durham, UK

ARTICLE INFO

Article history:
Received 3 June 2021
Received in revised form 4 March 2022
Accepted 15 March 2022
Available online 4 April 2022
Editor: R. Bendick

Keywords:
Canary Islands
edge-driven convection
hot spots
mantle convection

ABSTRACT

The Canary Islands hotspot consists of seven volcanic islands, mainly of Neogene age, rooted on oceanic Jurassic lithosphere. Its complex structure and geodynamic setting have led to different hypotheses about its origin and evolution, which is still a matter of a vivid debate. In addition to the classic mantle plume hypothesis, a mechanism of small-scale mantle convection at the edge of cratons (Edge Driven Convection, EDC) has been proposed due to the close proximity of the archipelago to the NW edge of the NW African Craton. A combination of mantle plume upwelling and EDC has also been hypothesized. In this study we evaluate these hypotheses quantitatively by means of numerical two-dimensional thermo-mechanical models. We find that models assuming only EDC require sharp edges of the craton and predict too narrow areas of partial melting. Models where the ascent of an upper-mantle plume is forced result in an asymmetric mantle flow pattern due to the interplay between the plume and the strongly heterogeneous lithosphere. The resulting thermal anomaly in the asthenosphere migrates laterally, in agreement with the overall westward decrease of the age of the islands. We suggest that laterally moving plumes related to strong lithospheric heterogeneities could explain the observed discrepancies between geochronologically estimated hotspot rates and plate velocities for many hotspots.

1. Introduction

Intraplate oceanic volcanism has been traditionally ascribed to deep thermal anomalies most likely associated with the upwelling of plume material. Oceanic islands would then form from decompression melting followed by melt ascent up to the surface. This simple view of a static plume beneath a moving plate (Morgan, 1971) can be further complicated by lithospheric-scale features such as the presence of steep lithospheric edges. The Canary archipelago is located in the vicinity of the western edge of the thick Northwestern African Craton (Fig. 1), representing, therefore, an excellent natural laboratory to study the interplay between plume upwelling and mantle flow associated with steep lithospheric edges. The Canary Islands consist of seven major volcanic islands rooted on Jurassic crust (150-170 Ma) adjacent to the northwestern margin of Africa (Fig. 1). The volcanic activity in the Canary archipelago shows a roughly westward age-decrease progression (e.g. Abdel-Monem et al., 1971; Carracedo et al., 1998), with the oldest subaerial volcanism in Fuerteventura (23 Ma) and the youngest (<2 Ma) in the westernmost islands of La Palma and El Hierro. The northeastern seamounts are in general older and exhibit an overall southwestward age-decrease trend (Geldmacher et al., 2005). Seamounts located to the southwest of the archipelago show ages varying from 142 Ma to 91 Ma (van den Bogaard, 2013) and do not follow a clear age progression.

The eastern islands, Fuerteventura and Lanzarote, are at the erosional stage and align parallel to the NW African margin. Together with the Conception bank, they form the East Canary Ridge (e.g. Ancochea et al., 2004 and references therein). The central islands, Gran Canaria, La Gomera and Tenerife, exhibit an E–W trend. Tenerife and Gran Canaria are in the post-shield stage with rejuvenated volcanism. The western islands, La Palma and El Hierro, are presently at a juvenile shield stage (Ancochea et al., 2004 and references therein). In spite of the different ages of formation, all the islands except La Gomera experienced activity during the Holocene, with historical activity recorded in the islands of Lanzarote, Tenerife and La Palma. The most recent eruptions are those of October 2011 – May 2012 close to the southern coast of El Hierro (e.g. López et al., 2012) and September - December 2021 in La Palma. Interestingly, the largest historical eruption of the

* Corresponding author at: Departamento de Física de la Tierra y Astrofísica, Facultad de CC. Físicas, Universidad Complutense de Madrid, Plaza de Ciencias 1, 28040 Madrid, Spain.
E-mail address: amnegred@ucm.es (A.M. Negredo).

https://doi.org/10.1016/j.epsl.2022.117506

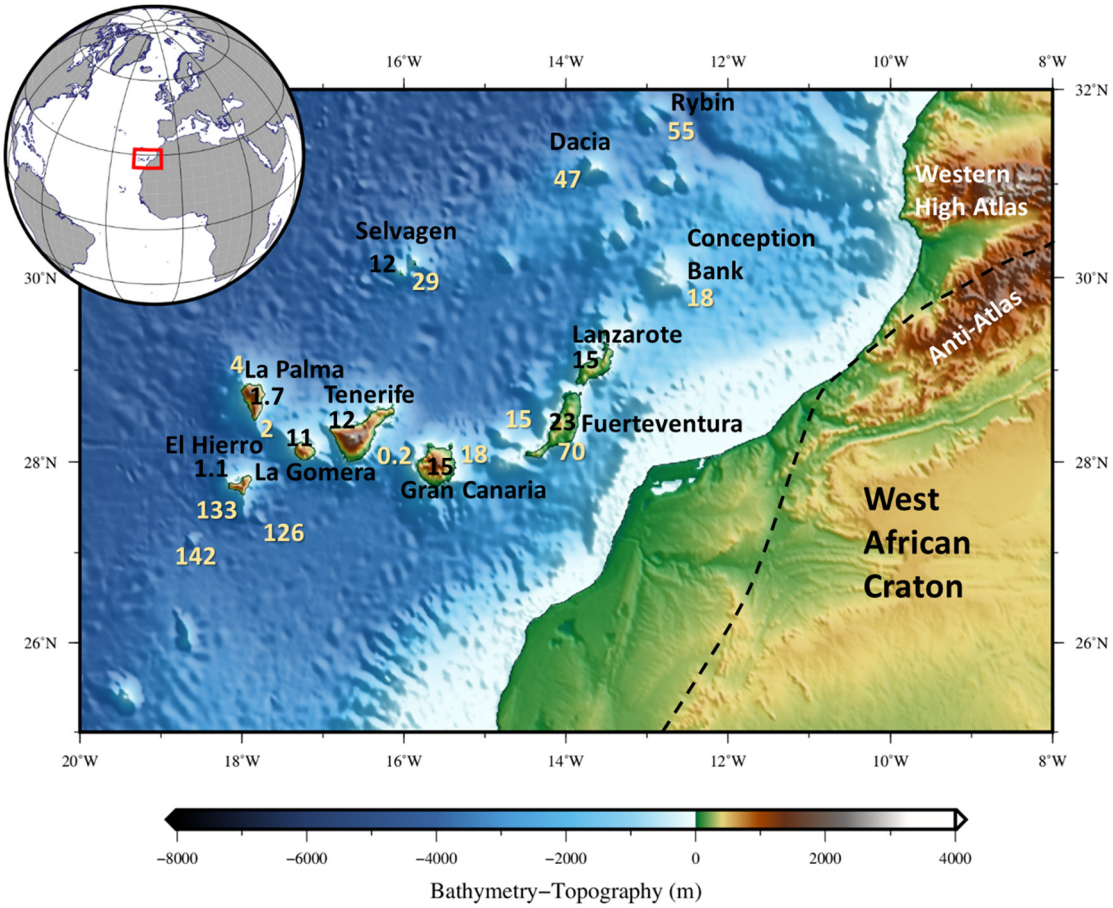

Fig. 1. Topographic/bathymetric map of the Canary Archipelago and northwestern Africa. Black numbers indicate the oldest age (in Ma) of subaerial volcanism and gold numbers stand for the ages of dated volcanic seamounts and ridges (see van den Bogaard (2013) for the original references for volcanic ages). The black dashed line indicates the edge of the West African Craton (from Ennih and Liégeois (2008)). (For interpretation of the colours in the figures, the reader is referred to the web version of this article.)

Canary Islands occurred at the opposite end of the archipelago: the 1730–1736 Timanfaya eruption on Lanzarote. In addition to the entire area of archipelago being magmatically active, other intriguing features for an intraplate volcanic chain are: i) the very long-lasting magmatic activity in the eastern island of Fuerteventura, where geological evidence and radiometric dating confirm the beginning of the magmatic activity as early as in the Late Cretaceous (Le Bas et al., 1986; Balogh et al., 1999), and ii) time spans as long as 25-30 My between shield and late stage volcanism for Fuerteventura and the Selvagem Islands (Le Bas et al., 1986; Geldmacher et al., 2001, 2005).

Fullea et al. (2015) modelled the lithospheric and upper mantle in the Canary Island using gravity field, surface elevation (isostasy) and seismic data within an integrated geophysical-petrologic approach. These authors predicted an only moderately thin lithosphere (about 110 km) beneath the archipelago, overlying an anomalous asthenosphere about 100 K hotter than the normal sub-lithospheric mantle. The P-receiver functions analysis by Martínez-Arévalo et al. (2013) found a low-velocity layer with $V_P/V_S > 1.81$ in the lithospheric mantle located at about 45–65 km deep. These authors associated the low velocity layer with the ubiquitous presence of melt beneath the islands.

A number of seismic tomography studies consistently find negative seismic velocity anomalies beneath the Canarian domain (Hoernle et al., 1995; Legendre et al., 2012; Miller et al., 2015; Civiero et al., 2018). Fig. 2 shows the shear wave velocity anomalies at 150 km depth from a recent surface wave tomography model (SA2019, Celli et al., 2020). The elongated negative velocity anomaly at sub-lithospheric depths beneath the Canaries and the Atlas Mountains is in strong contrast with the adjacent positive anomaly associated with the NW African Craton. This is highlighted in a vertical cross section (Fig. 2b), showing the contrast between the corresponding slow and fast seismic anomalies.

The complexity of the Canary Islands has led to a number of contrasting hypotheses proposed for its origin (see extensive review of earlier models by Anguita and Hernán, 2000). In addition to the classical mantle plume hypothesis, alternative models that could be categorized as 'tectonic' models include propagating fractures connecting the Islands to the Atlas Mountains in Morocco; compression-related block uplift leading to decompression melting, and magma escape during local rifting. Mantle plume or 'thermal' models are supported by the presence of low seismic velocity in the upper mantle, which is commonly interpreted in terms of a broad sub-lithospheric thermal anomaly, with a characteristic elongated shape ('sheet-like') extending through northwestern Africa to Europe (Fig. 2a). This pattern has been ascribed to mantle plume sub-lithospheric channeling (Oyarzun et al., 1997), or material flowing sub-horizontally northeastwards beneath Morocco from a Canary Island plume (Miller et al., 2015). Alternatively, edge-driven convection (EDC) has been proposed by King and Ritsema (2000) as a mechanism to explain intraplate volcanism on the African and South American plates. Following this mechanism, small-scale convection would develop in the upper mantle beneath the transition between oceanic lithosphere and thick cratonic lithosphere, due to thermal and rheological contrasts (e.g., Fig. 3). Interaction between EDC at the margin of the Northwestern African

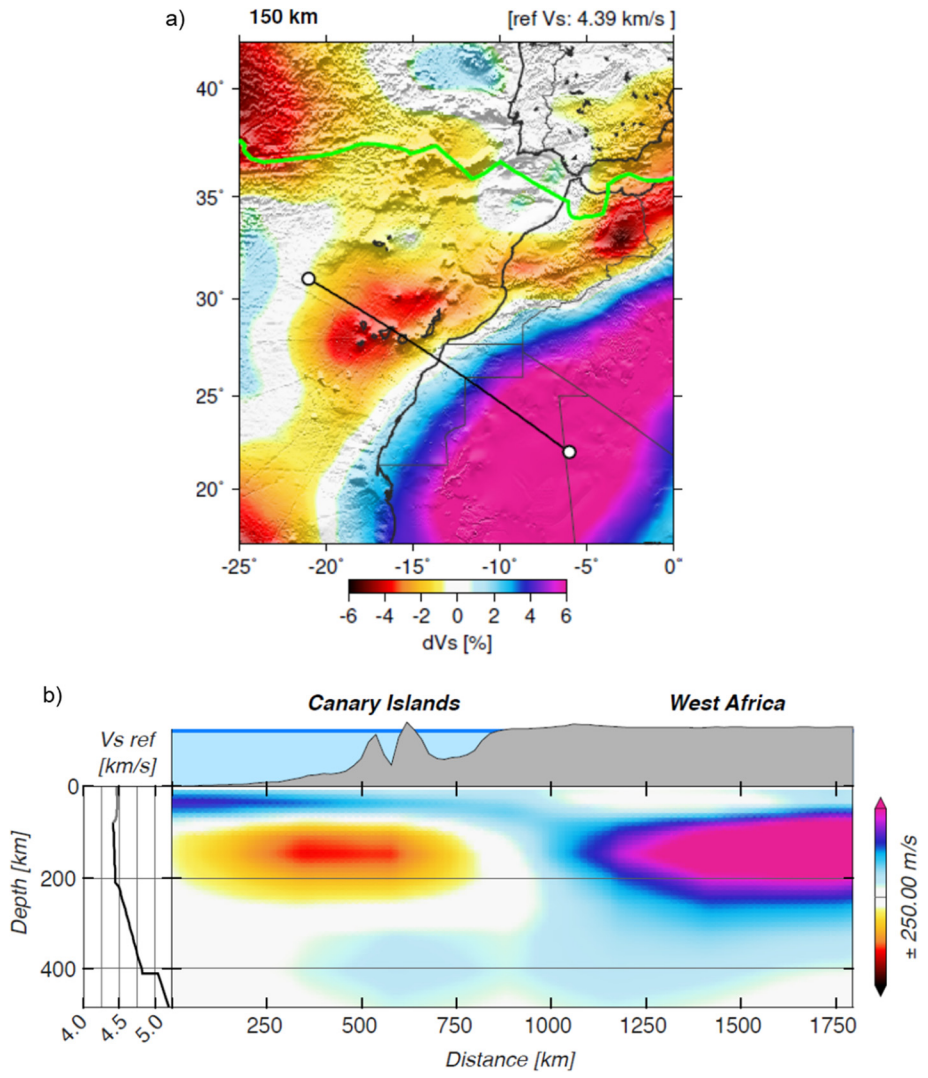

Fig. 2. a) S-wave velocity anomaly at 150 km depth, from the global seismic tomographic model by Celli et al. (2020). Black line indicates the location of the vertical section shown in panel b). This section highlights the contrasting seismic structure beneath the Canary Archipelago and the West African Craton.

Craton and an upwelling mantle plume (or blobs of plume material) has been proposed by Geldmacher et al. (2005) to explain the broad and irregular volcanic pattern in the Canary Islands (Fig. 1). The ability of these conceptual models (mantle plume, EDC or a combination of both) to explain the most prominent features characterizing the archipelago remains unclear. Among these features are the magmatic episodicity, the long lasting magmatism in the eastern islands (up to 70-80 Ma), and the westward island age decrease. Such age progression is at odds with the north to northwestwards slow absolute motion of the African plate during, at least, the last 20 Ma (e.g. Tetley et al., 2019 and references therein), and with negligible present-day motion due to the close location to the Euler pole (Wang et al., 2018).

In this study we perform geodynamic numerical simulations to evaluate different mechanisms, namely EDC and a combination of EDC and upper mantle plume upwelling. We compare our model predictions on partial melting and temperature distribution with the observed volcanic/magmatic patterns and upper mantle structure in the Canary Islands.

2. Methods

We model mantle dynamics resulting from the lateral thermal and rheological contrasts between the oceanic lithosphere and the NW African Craton, with and without an asthenospheric plume upwelling. To that aim we use the ASPECT modelling software (Kronbichler et al., 2012; Bangerth et al., 2020) to solve the equations of mass, momentum and energy conservation (eqs. (1)-(3)):

$$\nabla \cdot \boldsymbol{u} = 0, \tag{1}$$

$$-\nabla \cdot 2\mu\epsilon(\boldsymbol{u}) + \nabla p = \rho \boldsymbol{g}, \tag{2}$$

$$\rho C_p \left(\frac{\partial T}{\partial t} + \boldsymbol{u} \cdot \nabla T \right) - \nabla \cdot k \nabla T = \rho H + Q_{ad}, \tag{3}$$

where $\boldsymbol{u}$ is the velocity field, μ is the viscosity, $\epsilon(\boldsymbol{u})$ is the strain rate tensor, p is the pressure, ρ is the density, $\boldsymbol{g}$ is the gravity acceleration, C_p is the specific heat (1250 $\mathrm{J\,kg^{-1}\,K^{-1}}$), T is the temperature in K, k is the thermal conductivity (2.5 $\mathrm{W\,m^{-1}\,K^{-1}}$), H is radiogenic heat production per unit mass, and Q_{ad} is heat exchanged during adiabatic upwelling/downwelling. Here we assume a linear change of mantle density with temperature T as $\rho(T) = \rho_0(1 - \alpha(T - T_{ad}))$, where ρ_0 and T_{ad} are reference density (with a value 3300 $\mathrm{kg\,m^{-3}}$) and adiabatic reference temperature profile, respectively, and α is the thermal expansion coefficient (3.5×10^{-5} $\mathrm{K^{-1}}$). We do not account for pressure related density variations. Adiabatic heating is given by the expression $Q_{ad} = -\alpha\rho T \boldsymbol{u} \cdot \boldsymbol{g}$.

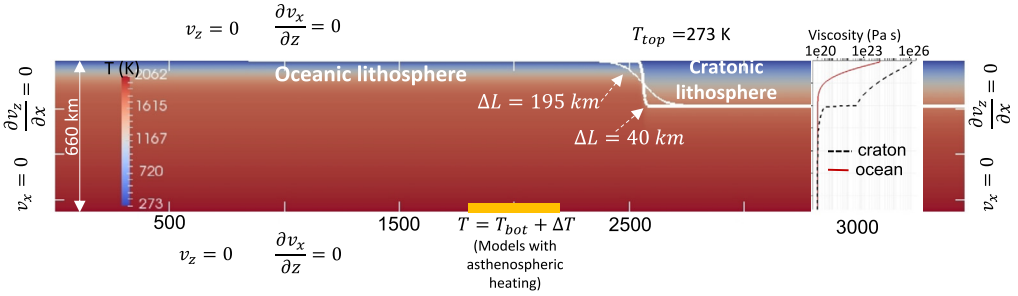

Fig. 3. Model setup showing the initial temperature distribution and boundary conditions, and the initial distribution of viscosity for oceanic (red line) and cratonic (black dashed line) lithosphere. The yellow rectangle denotes the portion of the bottom boundary where a temperature increment is applied in the series of models with asthenospheric heating. Two end member ocean-craton transition widths ΔL are represented, 40 and 195 km, which correspond to w values of 10 and 90 km, respectively in eq. (5).

ASPECT is an open-source code based on the finite element method that incorporates an adaptive mesh refinement strategy, allowing for a good resolution (highest resolution 2.3 × 2.3 km in this modelling) in zones of high temperature/viscosity gradients, and tracking of compositional contrasts that are advected with the flow.

Fig. 3 shows the model setup, boundary conditions and initial distribution of temperature and viscosity structure of a 2D generic vertical section roughly running from West (left) to East (right). The modelled domain is a two-dimensional Cartesian box extending 3960 km horizontally and 660 km vertically (aspect ratio 6). This wide box has been chosen after a number of tests to minimize boundary effects in the long-period simulations performed in this study. We have assumed a 2D approach and a closed modelling domain in a first attempt to analyze the interplay between upper mantle plume upwelling and EDC without further complexities. To a first order approximation, the 2D approach adopted here is consistent with the elongated shape of the seismic anomalies shown in Fig. 2.

The initial temperature distribution is an adiabatic gradient (0.5 K/km) for the asthenosphere, with a variable potential temperature $T_{ad,0}$, and conductive geotherm for the lithosphere controlled by the half-space cooling model:

$$T\big(z, A(x)\big) = T_{ad}(z) + (T_{top} - T_{ad,0})erfc\left(\frac{z}{2\sqrt{\kappa\, A(x)}}\right), \tag{4}$$

where z is depth and x is the horizontal distance from the left boundary. T_{top} is the surface temperature and $erfc$ refers to the complementary error function. κ is thermal diffusivity (here with constant value 0.8×10^{-6} m^2 s^{-1}; Katsura, 1995). $A(x)$ is the laterally variable cooling age. In order to simulate the lateral variations in the thermal state we use a young half-space cooling age for the oceanic lithosphere A_o in the left part of the model, and an old age for the craton A_c in the right part. The lateral change of these ages is defined by means of a hyperbolic tangent function $A(x)$ centred in the central point of the craton edge, x_c:

$$A(x) = A_o + \frac{A_c - A_o}{2}\left(1 + \tanh\frac{x - x_c}{w}\right), \tag{5}$$

where w is a parameter which controls the width of the transition between oceanic and cratonic lithosphere, ΔL (Fig. 3). This width will be varied in a series of simulations to analyse the effect of considering a smooth or sharp transition to cratonic lithosphere. For simplicity, we assume that the entire continental lithosphere is cratonic. We note that the age function $A(x)$ only defines the lithosphere thickness in the initial state (i.e. initial thermal conditions): later on during the model simulation the thermal thickness evolves dynamically in response to the numerically computed convection patterns.

The mechanical boundary conditions are free slip for all the boundaries, and boundary temperatures are maintained fixed at their initial values. The bottom temperature (T_{bot} in Fig. 3) is calculated using the initial adiabatic mantle geotherm. In the series of simulations accounting for plume-related heating, an increased temperature is imposed along a portion of the bottom boundary (right below the low Vs anomaly as mapped in Fig. 2) to force upper mantle upwelling material mimicking an upper mantle thermal plume. By imposing a barrier flow at the bottom boundary we are implicitly assuming that the Canary archipelago is a secondary hotspot (of asthenospheric origin following Courtillot et al., 2003), as we impede material inflow across the transition zone from the lower mantle into the upper mantle. This choice is based on the lack of continued tomographic anomalies in the lower mantle. For example, in the tomographic study by French and Romanowicz (2015) the lower mantle anomaly closest to the Canary archipelago is located about 1000 km southwards coinciding with the surface location of the Cape Verde hot spot.

We adopt a linear rheology with a viscosity that depends on temperature and on composition:

$$\eta(T, c) = \eta_0 e^{-\beta(T - T_{ad})/T_{ad}}\zeta(c), \tag{6}$$

where η_0 is the reference viscosity; β is the thermal viscosity exponent defining the dependence on temperature; and $\zeta(c)$ is the compositional pre-factor for the viscosity. In order to simulate the high strength of the depleted and dehydrated lithosphere of the NW African Craton we define a specific compositional field, and impose an increase of two orders of magnitude, $\zeta(c) = 100$, in the viscosity in a block on the right side of domain, extending to a depth $z = 200$ km (Fig. 3). The left boundary of this viscous block has a shape given by a hyperbolic tangent function analogous to the age function $A(x)$. The compositional pre-factor equals 1 for the rest of the model domain. After performing a series of tests, a value for the thermal viscosity parameter $\beta = 12$ and a reference viscosity $\eta_0 = 10^{20}$ Pa s have been selected for reference models as they lead to the formation of a stable stagnant lid with a thermal thickness of about 110 km (with thermal LAB defined by the 1315 °C isotherm), as modelled by Fullea et al. (2015) for the Canary Islands lithosphere. Moreover, these values yield a similar viscosity profile as that used in the modelling by Kaislaniemi and van Hunen (2014), who assumed a linear rheology and adopted low activation energy values (E<200 kJ mol^{-1}) to 'mimic' a non-linear rheology. Similarly, Christensen (1984) showed that reducing the activation enthalpy for a Newtonian formulation produces similar convection patterns as a non-linear rheology with normal activation enthalpy. The reference model assumes a sharp ocean-craton transition $\Delta L = 40$ km (corresponding to $w = 10$ km in eq. (5)), reference viscosity $\eta_0 = 10^{20}$ Pa s, thermal viscosity exponent $\beta = 12$, craton rheologic thickness of 200 km and initial ages $A_o = 60$ Myr and $A_c = 250$ Myr. The craton thickness of 200 km

is an approximated average between different tomographic models (e.g. Celli et al., 2020; Fig. 2b), passive source seismics (Fishwick and Bastow, 2011) and the integrated modelling of elevation, geoid and thermal analysis by Globig et al. (2016). Here we adopt relatively high potential temperature values $T_{ad,0} \geq 1427\,^{\circ}C$, which is within the range of other hotspots associated with mantle plumes. For example, Herzberg and Asimow (2008) obtained estimates to $1450 \pm 10\,^{\circ}C$ and $1560 \pm 40\,^{\circ}C$ for Iceland and Hawaii, respectively.

Given the described initial state, mantle flow will be driven by the lateral thermal and rheological contrasts between oceanic and cratonic lithosphere. However, this initial state is not realistic since convection has not developed yet. The problem of how to deal with a representative initial state is widely discussed by Sleep (2007) and Kaislaniemi and van Hunen (2014). A common procedure is to leave the simulation run for tens or even hundreds of Myrs until a statistical steady state (i.e. steady state when averaged over several tens of Myrs) develops. We follow this procedure in this study to select a representative state that will be different for purely EDC models and for upper mantle plume models (see Results section).

Our upper mantle model setting does not simulate the dynamic interaction with the lower mantle, and therefore has no basal thermal boundary layer to sustain high internal mantle temperatures such as those in a plume context. For that reason we follow the approach by (Kaislaniemi and van Hunen, 2014) of adopting high radiogenic heat production values to maintain a stable and realistic mantle potential temperature during the long duration of the simulations. We have checked that this is achieved with heat production values of $H = 16 \times 10^{-12}\ W\,kg^{-1}$ (about two times higher than the present-day mantle value of $7.38 \times 10^{-12}\ W\,kg^{-1}$; Schubert et al., 2001) for purely EDC models, and $H = 12 \times 10^{-12}\ W\,kg^{-1}$ for plume models.

In this study we estimate the amount of melt by means of the 'passive advection approach' described by Gassmöller et al. (2016; see their supplementary information). A compositional field F_{max}, maximum melt fraction, is introduced to estimate the maximum degree of melting in any point. We have created a new 'material model' extension in ASPECT for this purpose. This extension incorporates the dry peridotite melting parameterization of Katz et al. (2003) (see melt fraction functions and parameters in appendix C in Dannberg and Heister, 2016). This parameterization is used to update the F_{max} field only when the stored value of maximum degree of melting is exceeded. In this way, we limit melting by indirectly accounting for depletion. This compositional field is passively advected with the mantle flow. This approximation would be valid only in the limit of very low porosity, so that the solid and porous flow have the same velocity. Similarly, this approximation of passive advection of melt with the flow becomes less appropriate the further away melt is advected from its source region. We do not consider melt extraction or freezing, and we have not included latent heat of melting in the energy equation (eq. (3)). These simplifications lead to an overestimation of the amount of melt. The simplified procedure to estimate melting is intended to obtain first-order estimates of the region of melting, rather than accurate amounts of melting.

3. Results

In the following we show the results of two series of models: i) EDC only models, and ii) EDC plus plume models. In the first series of models we analyse the conditions for melt generation when only lateral thermal and rheological contrasts between the oceanic and the cratonic lithosphere are imposed. In the second series, the 'upper mantle plume' models, we take into account a temperature increase along part of the bottom boundary (yellow segment in Fig. 3) to induce upper mantle plume upwelling. We will discuss the ability of these model series to reproduce widespread melting, westward migrating magmatism and the presence of a sublithospheric thermal anomaly.

3.1. EDC only models

We model EDC dynamics using a reference simulation for a potential temperature $T_{ad,0} = 1720$ K. Additional tests show that no melting is generated for lower values of potential temperatures. At the beginning of the simulation, large initial instabilities appear as the convection cells are being created, and later on the system evolves towards a relatively stable regime (supplementary Video 1) which can be considered as appropriate to analyse the patterns of EDC. The transition to this regime is identified by analysing the time evolution of the root mean square of the velocity (v_{RMS} plot in Fig. 4a). After some 130 Myrs v_{RMS} tends to more stable values (although not in completely steady-state, as shown by the v_{RMS} long-term upwards trend) when the average thickness of the lithosphere changes very little (less than 0.5 km every 10 Myr). Fig. 4b shows the evolution after attaining this stable stage. The melting area is mainly restricted to a narrow area of about 200 km width adjacent to the craton edge.

To analyse melt related to EDC and not any other small-scale instabilities, we have defined an integration domain close to the craton edge as a box $0 < z < 260$ km and $2000\ km < x < 2700$ km. The integrated melt volume through time is plotted in Fig. 5 for models with different widths of the ocean-craton transition ΔL, controlled by the parameter w in eq. (5) (ΔL values of 40, 125, 165 and 195 km, correspond to w values 10, 50, 70 and 90 km, respectively). The equivalent plot for the melting rates (time derivatives of melt volume) is shown in supplementary Figure S1. After a phase of fast melt generation a stable phase with episodic small pulses of melt generation develops (note that small decreases of the integrated melt, or negative values of the melting rates, are due to melt being transported out of the integration domain), similarly to the EDC modelling in the Atlas by Kaislaniemi and van Hunen (2014). For the model shown in Fig. 4 ($\Delta L = 40$ km) the frequency of these pulses is ~25 Myr and peak maximum rates of 3 km^2/Myr (supplementary Figure S1).

Models with exactly the same characteristics and parameters, but with a more gradual ocean-craton transition (higher ΔL values) produce significantly lower amounts of melt and a reduced frequency of melting pulses. The simulation with transition width of $\Delta L = 195$ km (geometry shown by the thin white line in Fig. 3) generates almost no melt (purple line in Fig. 5), thus revealing how important this geometric parameter is. The reason for this dramatic melting decrease for smooth ocean-craton transitions is that edge convection is much less vigorous. In order to produce some melting with this model geometry, a warmer mantle with a potential temperature $T_{ad,0} = 1740$ K is required. In this model, melting develops preferentially close to the craton edge, but it spreads away, transitioning to small scale convection melting, without any new melting pulses occurring in this corner (green line in Fig. 5 and supplementary Video 2).

3.2. EDC plus plume models

In a second set of models we force the upwelling of hot material in the upper mantle by modifying the basal thermal boundary condition imposing an increase of temperature ΔT along a portion 400 km long of the bottom boundary (yellow segment in Fig. 3). This segment is centred at $x = 2000$ km, which corresponds to the approximated location of the centre of the low Vs anomaly with respect to the location of the craton edge (see Fig. 2 for geometric constraints on the model setup). The segment with increased temperature at the bottom boundary is chosen so wide to allow for the plume tail to move laterally.

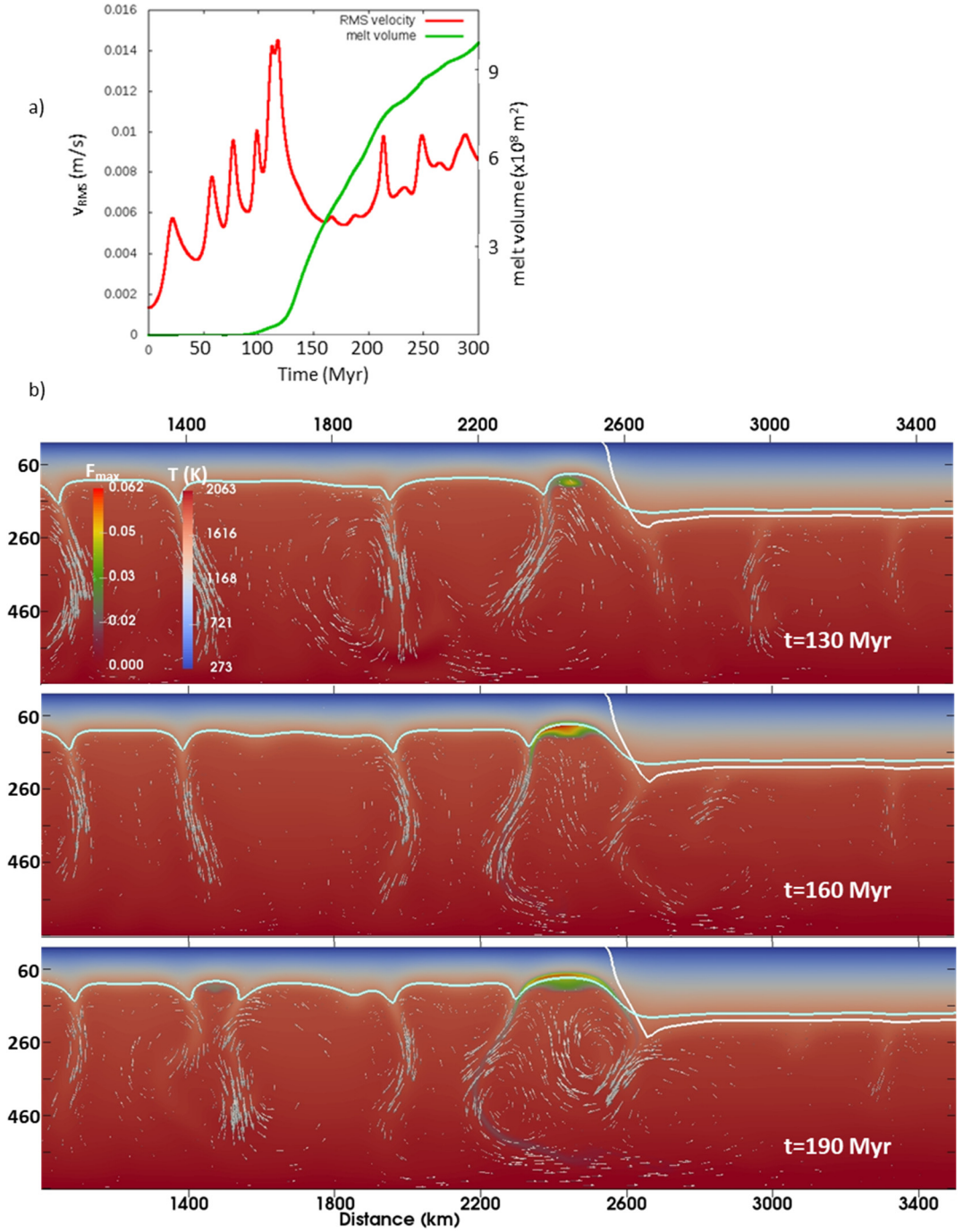

Fig. 4. a) development of the root mean square velocity v_{RMS} (red line) and melt volume (actually melt area in our 2D approach; green line) integrated in the entire model domain, for a reference simulation that only considers edge-driven convection. b) model development once the unrealistic initial state has vanished (no vertical exaggeration). Colours denote the temperature distribution and the maximum melt fraction compositional field. Arrows depict the velocity field. The light blue contour indicates the 1315 °C isotherm, as representative of the thermal lithosphere-asthenosphere boundary.

3.2.1. Effect of the basal temperature increase

We have performed a first simulation with exactly the same geometric, thermal and rheological characteristics as the purely EDC model shown in Fig. 4, except for a temperature increment $\Delta T = 200$ K applied along a part of the bottom boundary. Again, we allow for long simulations to be sure that the artificial initial state has evolved to a more representative temperature distribution. Therefore, we only interpret the melting that occurs during this stable (or pulsating) upwelling regime. The RMS velocity and convection pattern evolution show that this sets in after about 110 Myr from the beginning of the simulation (supplementary Video 3; note that the pulsating upwelling is always transient). We represent in Fig. 6 different snapshots of this simulation.

The geometry of the generated upper mantle plume is highlighted by the temperature contour (pink line) of 60 K above the mantle adiabat. The sub-lithospheric melting area progressively widens westwards (leftwards), reaching a width of about 400 km at 130 Myr, in contrast with the maximum width of the melting region of about 200 km for the EDC model shown in Fig. 4. The averaged melting rate for this model in the analysed period is ~10 km^2/Myr (see curve with $T_{ad,0} = 1720$ K in supplementary Figure S2), about three times higher than the maximum rate for

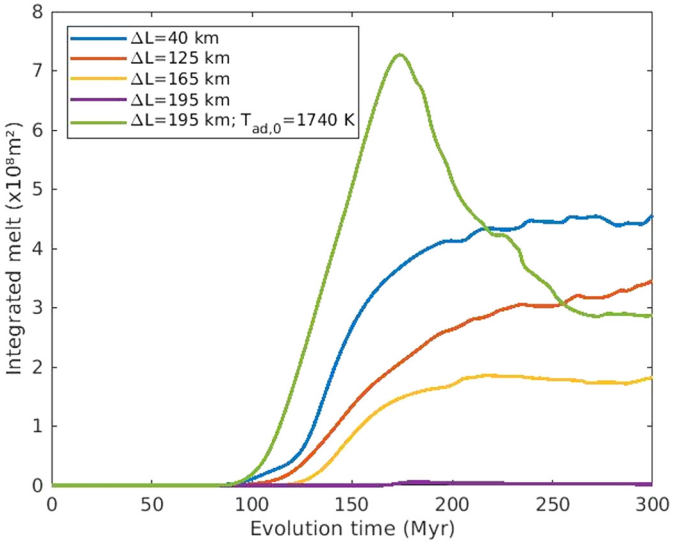

Fig. 5. Development of the integrated melt volume (melt area in this 2D approach) for EDC models assuming different widths of the transition between the oceanic and the cratonic lithosphere ΔL. Maximum melt fraction is integrated across part of the model domain ($z < 260$ km and 2000 km $< x <$ 2700 km) that contains the area adjacent to the craton edge. The reference simulation shown in Fig. 4 is indicated by the blue line. All models except the one represented by the green line assume a potential temperature $T_{ad,0} = 1720$ K. Note that negligible melt is generated when a smooth ocean/craton transition is assumed (purple line, $\Delta L = 195$ km; rest of parameters as in the Reference Model). Note: the decrease of melt volume is due to melt being advected out of the integration model domain.

the equivalent purely EDC model. However, caution must be taken with this comparison provided that the average temperature of the model domain increases with time due to the basal temperature increment (potential temperature and heat production are exactly the same as in the EDC model). For this reason, we have defined a slightly colder reference model, as explained in the following subsection.

3.2.2. Models combining plume upwelling and EDC

In order to analyse in detail the evolution of combined EDC and upper mantle plume upwelling, we have defined a Reference Model (RM) with a lower potential temperature $T_{ad,0} = 1700$ K, and a radiogenic heat production $H = 12 \times 10^{-12}$ W kg^{-1}, suitable to maintain a stable average temperature. The long-term (300 Myrs) evolution of this model is shown in supplementary Video 4. Fig. 7 illustrates the differences in convection patterns between this RM, with plume upwelling beneath a laterally heterogeneous lithosphere containing a cratonic edge (RM; Fig. 7a-c), and a model with a homogeneous lithosphere with the same characteristics as the oceanic domain in the RM (Fig. 7d-f).

For the RM, the flow pattern is asymmetric because the downwellings to the sides of the rising plume do not occur simultaneously. The mantle flow in this model changes with time from a dominantly clockwise cell to the east (right) of the axis plume (see plot at 125 Myr in Fig. 7b) to counter-clockwise flow to the west (left) of the asthenospheric plume (see plot at 150 Myr in Fig. 7c). The deflection of the plume tail changes from eastwards to westwards. This evolution towards counter-clockwise flow does not occur for the model with a homogeneous lithosphere (Fig. 7d-f), displaying always a symmetric geometry with clockwise flow to the east of the plume axis, counter-clockwise to the west and a vertical plume tail. The fixity of the plume tail beneath this homogeneous lithosphere model makes it much more efficient to heat up, weaken and thin the upper part of the asthenosphere and the base of the lithosphere. Therefore, the amount of melt is much larger in this model (Figs. 7 and 9). The lateral motion of the plume tail in the RM model causes a westward migration of the asthenospheric thermal anomaly. For example, the contour showing the 50 K excess temperature (above the mantle adiabat) migrates about 300 km westwards between 125 and 150 Myr for the RM (pink contour in Fig. 7a).

We have performed a series of tests to analyse the effect of different parameters, namely basal temperature increment ΔT, the reference viscosity η_0 and the thermal viscosity exponent β, on the thermal field, upper mantle flow, and melt fraction and distribution. Four of these tests are compared at the same model time, 150 Myr, in Fig. 8. We have checked in the RMS velocity plots that the large instabilities related to the artificial initial state have disappeared by this time in all the simulations. The RM (Fig. 8a; $\eta_0 = 10^{20}$ Pa·s; $\Delta T = 200$ K; $\beta = 12$) generates a maximum melt fraction of 2% at 150 Myr (3.3% for the model with a homogeneous lithosphere shown in Fig. 7d-f), while this amount increases to 11% in the case of a basal temperature increment of $\Delta T = 250$ K (Fig. 8b). Increased melting is a response to more effective asthenospheric heating, as evidenced by the 75 K excess temperature reaching shallower depths (compare Figs. 8a and 8b). Compared to the RM, models with a lower reference viscosity, $\eta_0 = 5 \cdot 10^{19}$ Pa·s, (Fig. 8c) are able to generate more melt, 7.5% at the base of the (weaker) lithosphere but the high mobility of the plume makes it less effective to heat up large regions of the base of the lithosphere and upper part of the asthenosphere. In order evaluate the effects of a viscosity reduction at sublithospheric depths, we have performed an additional simulation with the same parameters as in the RM, but with a lower value of the thermal viscosity parameter, $\beta = 11$ (Fig. 8d). Faster lateral westward migration of the mantle plume occurs; at 150 Myr, the area of the second melting pulse is about 300 km wide and a maximum melt fraction is about 4%, two times higher than in RM (compare Figs. 8a and 8d). Given the simplified procedure to estimate the melt fraction (see Section 2) and the fact that these models are, by their very nature, not steady state, the maximum melt fraction values for the different simulations should only be considered in relative terms to compare the models capability to produce melting. This sensitivity study also reveals that the progressive evolution towards a large counter-clockwise cell and the subsequent westward migration of the thermal anomaly and melting region is a robust feature in all these simulations (see supplementary Videos 4-7).

Fig. 9 shows the sensitivity of integrated melt volume evolution over the entire model domain to different parameters. The basal temperature increment ΔT and reference viscosity are shown to exert the strongest influence on melting rates (for the ranges of variation of the tested parameters). This figure also shows that the model with a flat lithosphere (green line in Fig. 9) produces more melt than the RM. Also melting rates are higher and exhibit an overall increasing trend (supplementary Figure S2).

4. Discussion

4.1. Purely EDC models

The series of simulations to model EDC show that melting occurs if a relatively sharp cratonic edge and an elevated potential temperature ($T_{ad,0} > 1720$ K in these simulations) are assumed. These two requirements would explain why not all cratons are bounded by magmatic regions. The geometry of the craton edge is an important factor controlling the occurrence of EDC-related partial melting according to our results. The actual width of the West African craton edge is hard to constrain, as seismic tomography models and lithospheric modelling based on thermal, geoid and elevation data (Globig et al., 2016) usually do not have enough resolution and are affected by choices in lateral regularization. Most previous EDC studies have assumed a vertical ge-

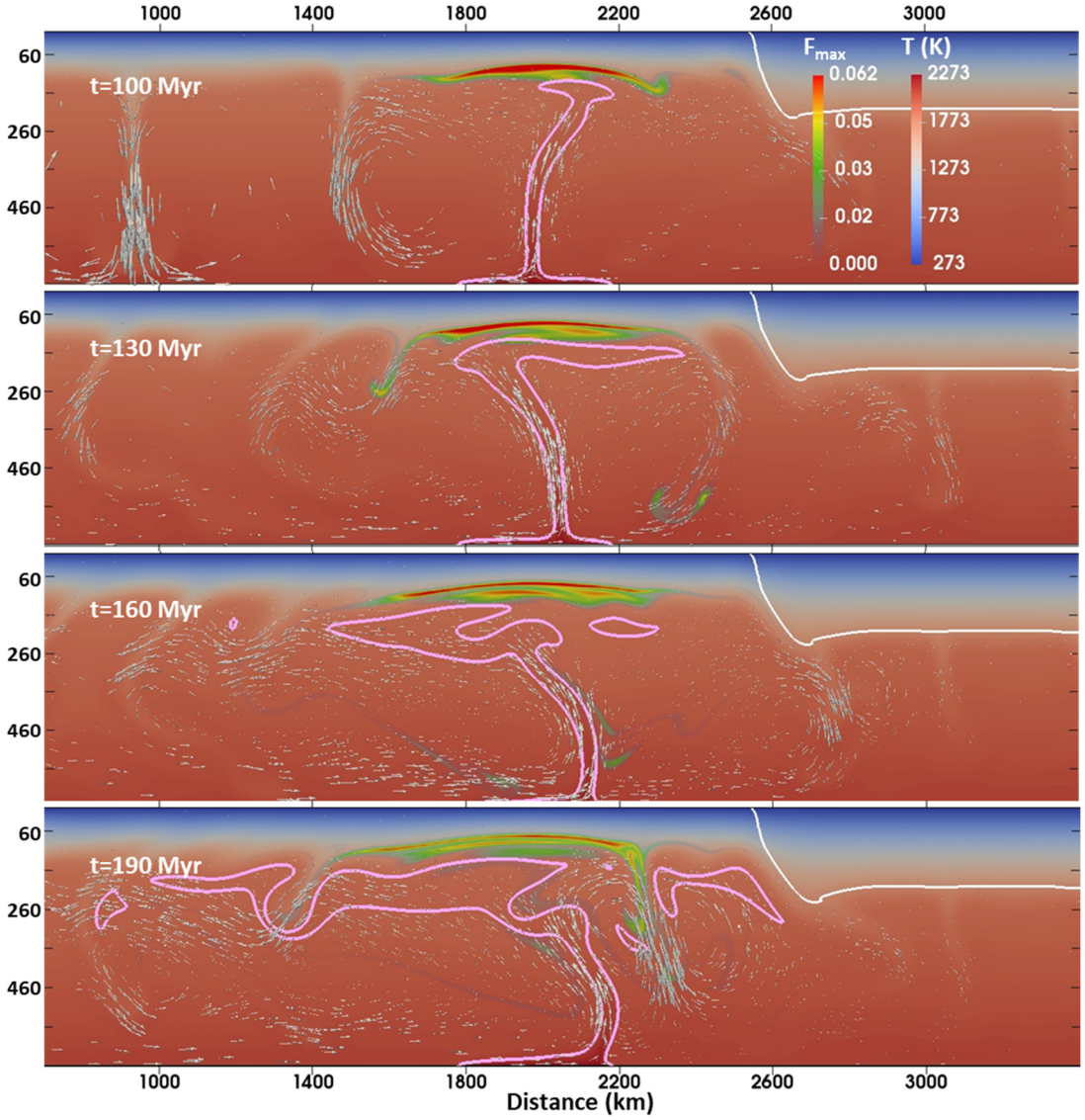

Fig. 6. Model development for a simulation with the same model setup as the EDC model in Fig. 4, but with a temperature increment of 200 K along a portion of the bottom boundary. Colours denote the temperature distribution and the maximum melt fraction compositional field. Arrows depict the velocity field. Pink contour represents the 60 K excess temperature with respect to the mantle adiabat.

ometry for the edge of the thick, cratonic lithosphere (King and Anderson, 1995, 1998; Shahnas and Pysklywec, 2004; Kaislaniemi and van Hunen, 2014). However, geodynamic models of craton margin preservation by Currie and van Wijk (2016) indicate that very strong cratons are needed to maintain steep transitions. Kim and So (2020) showed the effect of edge geometry on the EDC cell pattern and dynamic topography but they only showed melt distribution for a craton edge as narrow as 30 km. In contrast, the recent systematic EDC study by Manjón-Cabeza Córdoba and Ballmer (2021) tested different craton edge widths between 132 and 396 km and found that for models predicting EDC-related melting, this melting only occurs for a short time span. They predicted persistent melting only for models where EDC transitions into widespread melting due to sublithospheric small scale convection (similar to our EDC simulations with wide craton edges and high potential temperature; green line in Fig. 5). They performed a test mimicking the Canary Islands using an ocean-craton transition as wide as 528 km and did not obtain any melting. In our modelling we have explored the range from sharp to smooth craton edges (from 40 to 195 km transition widths) and we have found a transition from sustained and localized melting for steep craton walls, to transient melting or widespread small scale convection (Fig. 5) for warm models with gradual ocean-continent transitions. Perhaps the models by Manjón-Cabeza Córdoba and Ballmer (2021) would also provide sustained melting for steeper craton edges.

Predictions for purely EDC models favour the occurrence of melting in a narrow area (about 200 km wide) adjacent to the craton edge (Fig. 4), which is in contradiction with the occurrence of volcanism at distances $>$ 700 km from the craton edge (see for example the distance between El Hierro Island and approximated location of West African Craton edge in Fig. 2). Here we show that EDC only simulations generate small EDC cells unable to generate any large thermal anomaly beneath the oceanic lithosphere. Therefore, EDC only models would be inconsistent with the presence of negative seismic velocity beneath the Canary Islands lithosphere (Fig. 2) and with the temperature model inferred from geophysical-petrological multi-data modelling by Fullea et al. (2015). On the other hand, the formation of partial melting adjacent to the craton edge resembles the pattern found by Kaislaniemi and van Hunen (2014) and gives further support to the hypothesis of EDC-related Cenozoic volcanism in the Atlas Mountains, as orig-

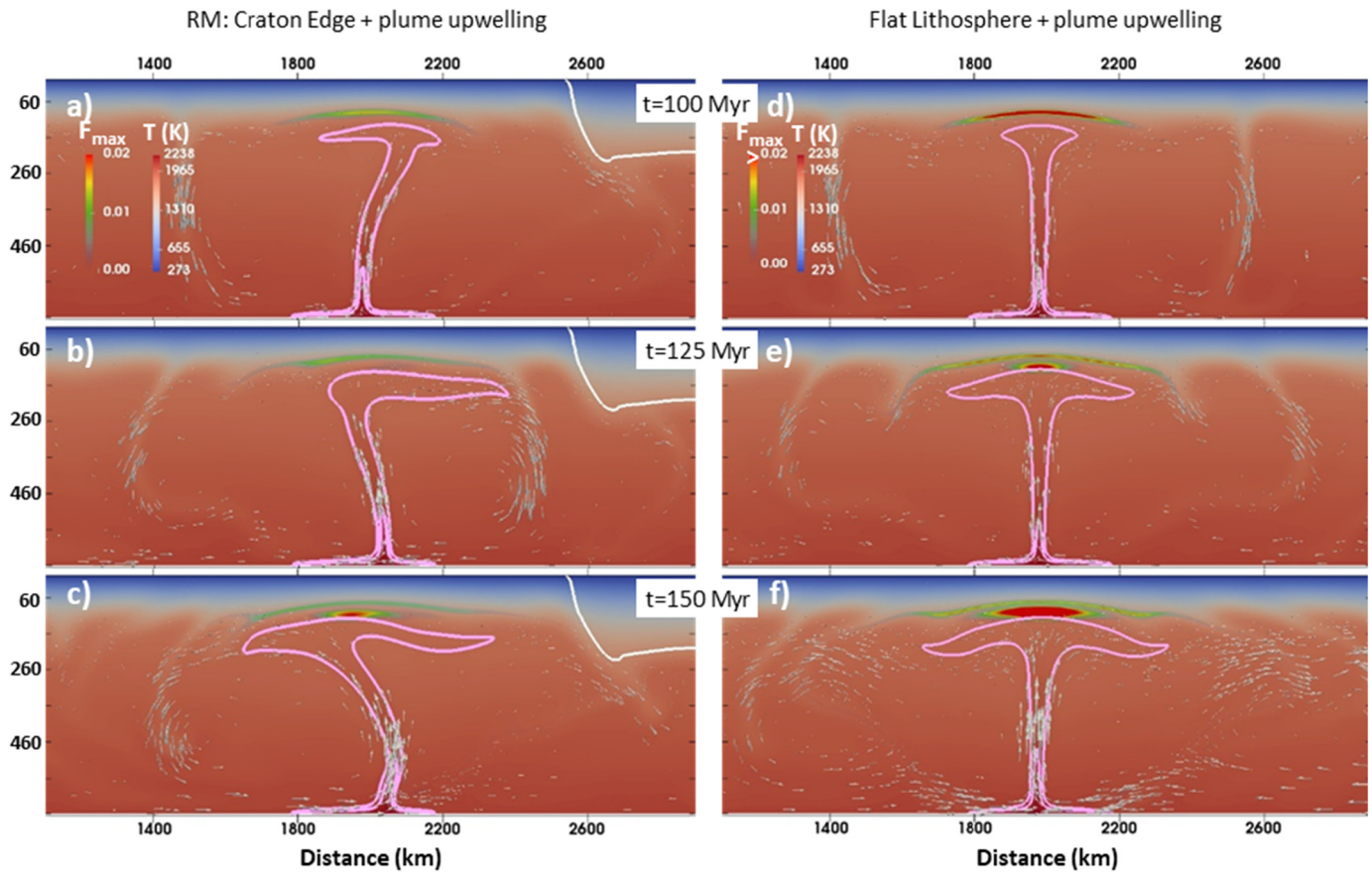

Fig. 7. Time evolution of (left) the Reference Model (RM), which considers a combination of EDC associated with a craton edge, and forced asthenospheric upwelling; and (right) a model that only differs from RM in that it incorporates a homogeneous lithosphere. This comparison reveals that the main effect of having a strong lithospheric contrast is the westward migration of the upper mantle plume. Colours show the temperature distribution, and the maximum melt fraction compositional field. Pink contours show the 50 and 100 K excess temperature with respect to the adiabat distribution. Arrows depict the velocity field.

inally proposed by Missenard and Cadoux (2012). Our results for narrow craton edges predict a sustained melting with long-term periodic pulses every 20-25 Myr approximately (Fig. 5 and supplementary Figure S1). Interestingly, Kaislaniemi and van Hunen (2014) found a 14-26 Myr melting period using a different model setup. This is consistent with the hypothesis of melting episodicity as an inherent and robust feature of EDC close to narrow craton edges.

4.2. Models combining EDC and upper mantle plume upwelling

Models incorporating the upwelling of upper mantle material produce wider thermal and melting anomalies according to our results. This is in better agreement with melting anomalies in the sub-Canarian mantle across the entire archipelago. A comparison between models assuming a homogeneous lithosphere and those with ocean/craton lateral contrasts (Fig. 7) reveals that this second structure causes a lateral migration towards the ocean of the plume in the analyzed timespan, which is consistent with the overall westward decrease of the age of the islands. This lateral migration is a robust feature as it is reproduced in all the simulations combining EDC and plume upwelling. It occurs faster for lower reference viscosities, but there is less asthenospheric heating in that case (Fig. 8c), which is at odds with the prominent low Vs anomaly (Fig. 2) and with the anomalously hot asthenosphere with an excess temperature of about 100 K found in the combined geophysical and petrological modelling by Fullea et al. (2015). From the sensitivity test shown in Fig. 8 we infer that such a high excess temperature requires basal temperature increments $\Delta T > 250$ K, which would be also consistent with the ubiquitous presence of melt beneath the islands proposed in the RF study by Martínez-Arévalo et al. (2013). Instead, the RM underestimates the lateral extent of both the thermal anomaly and the region of partial melting (Fig. 7a-c).

All simulations show episodic melting reactivations with irregular periods varying between 20 and 40 Myr, which mostly occur in the eastern part of the anomaly. This non-periodic behaviour is related to the complex interaction between the upwelling plume and the convection at the craton edge. We speculate that these predicted melting pulses are consistent with the long magmatic history of the easternmost island of Fuerteventura (Le Bas et al., 1986; Balogh et al., 1999). As discussed by Le Bas et al. (1986), it could be possible that other islands have a similar early history but evidence is not exposed due to the lack of erosion.

The comparison between models of plume upwelling beneath strongly heterogeneous or homogeneous lithosphere (Fig. 7) can explain why mantle plumes beneath roughly homogeneous oceanic lithosphere, as in the Hawaii hotspot, produce linear trends in volcanism and high buoyancy fluxes, while 'swaying' plumes caused by plume interaction with EDC can result in more irregular magmatic patterns both in space and time. Even for the paradigmatic example of Hawaii, the modelling by Ballmer et al. (2011) showed that the interaction between the plume and the pre-existing washboard topography created by small-scale convection at the base of the plate causes the plume to spread and melt asymmetrically, as well as temporal variations of the volcanic flux.

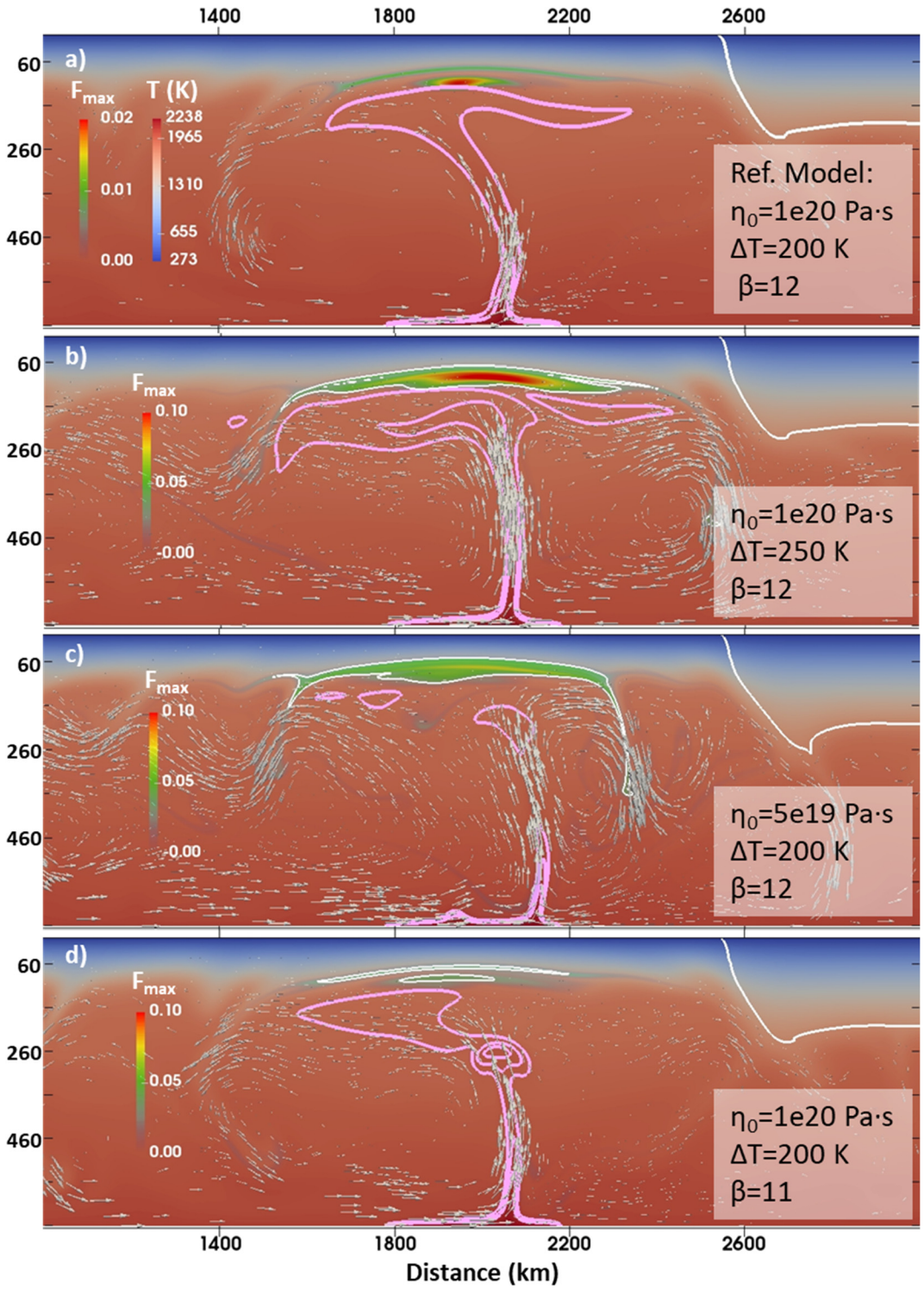

Fig. 8. Comparison between different models at 150 Myr, showing the effects of changing the temperature increment ΔT applied along a portion of the bottom boundary, the reference viscosity η_0 and the thermal viscosity exponent β (note the different colour scale for maximum melt fraction in the upper panel to facilitate the visualization of the melting region). White contours outline the region with maximum melt fraction $>$ 0.03 (3%). Pink lines show the 50-, 75- and 100-K excess temperature contours.

4.3. Model limitations

All models make a number of simplifying assumptions and approximations. The limitations of our simplified modelling should be taken into account when interpreting the results. While mantle plume upwelling is an intrinsically 3D process, we consider that the 2D approach adopted in this study is consistent, to a first order, with the elongated and roughly parallel shape of the fast and slow seismic anomalies in the area (Fig. 2a). The development of a counterclockwise cell and the subsequent westward migration of the asthenospheric thermal anomaly is likely maximized by the adopted 2D approach. However, we expect the qualitative result of plume migration away from the craton edge, or towards areas of low relatively thin lithosphere, to be valid for 3D configurations with upper mantle upwelling occurring close to the craton edge. 3D effects need to be incorporated in future studies accounting for

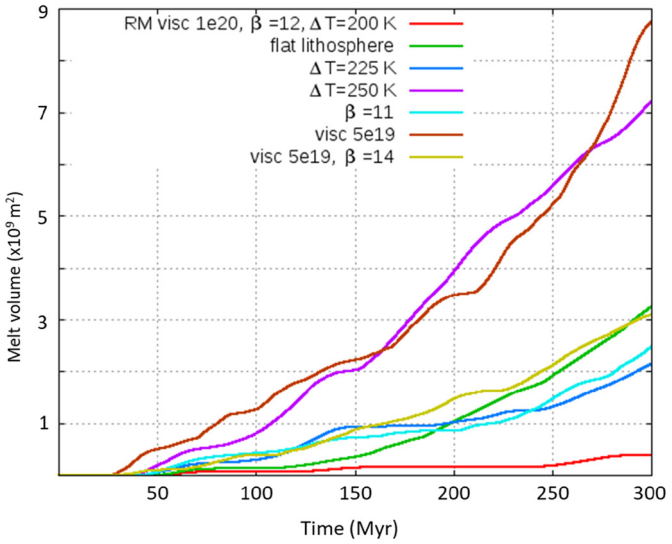

Fig. 9. Development of the integrated melt volume (melt area in this 2D approach) for models combining EDC and upper mantle plume upwelling. Maximum melt fraction is integrated over the entire model domain. The Reference Model (RM) is indicated by the red line. The text in the legend indicates the parameter that is modified with respect to RM. Viscosity values in the legend denote reference viscosity η_0 in Pa·s.

the motion of the African plate and 3D structures of the oceanic and continental domains. Prominent examples of this type of 3D modelling are the mantle plume-ridge interaction studies of the Réunion hot spot by Bredow et al. (2017) and the Tristan plume by Gassmöller et al. (2016).

The simplified procedure used in this study to estimate the melt amount is still useful for comparison purposes between different simulations and to obtain a first-order estimate of the melting region. Future work is needed to obtain more accurate values of melt volume, melt migration, and melting rates. This would involve two-phase porous media flow modelling, which is numerically challenging and requires a large number of parameters that are poorly constrained for the Canary region.

Another simplification adopted in this study is the linear temperature- and composition-dependent rheology (Eq. (6)). This simple viscosity structure facilitated finding the combination of reference viscosity η_0 and thermal viscosity exponent parameter β that leads to the development of a stagnant lid with the characteristics of the Canary Islands lithosphere. The simplified viscosity profile (eq. (6)) does not include the dependence with pressure and activation volume, which would lead to a viscosity increase with depth. The effect of including this increase is a reduction of the convection cells size, but the qualitative result of a laterally migrating plume will be likely the same as long as the viscosity values at 100-400 km depths are similar.

4.4. Implications for absolute plate motion estimates

Here we have imposed a fixed plate and conducted EDC simulations in which we find 10-20 mm/yr westwards migration of the plume-related asthenospheric thermal anomaly, roughly perpendicular to the absolute plate motion of Africa. Our results thus illustrate that assuming fixed plumes may not always be a valid approach, in particular for heterogeneous, slow moving plates. Volcanic age progression combined with the assumption of a fixed plume can lead in these cases to wrong estimates of absolute plate motion, both in magnitude and direction. The recent model by Wang et al. (2018) finds plate velocities significantly lower than the observed rates of hotspot volcanic migration. They specifically mention that the rate of 20 ± 4 mm/yr for the Canary hotspot based on the $^{40}Ar/^{39}Ar$ dating and the 55 ± 8 mm/yr rate jointly determined by the K–Ar and $^{40}Ar/^{39}Ar$ data for the Galapagos hotspot are significantly higher than plate velocities in their absolute plate motion model. Wang et al. (2018) suggest that the systematic discrepancy between hotspot volcanic migration rates and plate velocities cannot be fully explained by K–Ar age measurements errors and claim that other mechanisms leading to the bias towards higher hotspot rates should be investigated. On the basis of the present study, a possible mechanism for this bias in the Canary hotspot could be the migrating asthenosphere temperature anomaly caused by shallow mantle flow due to lateral lithospheric thickness variations. Interestingly, the modelled migration away from craton edges, towards areas of relatively thin lithosphere, is consistent with the conclusion by Wang et al. (2018) of hotspots moving towards mid-ocean ridges.

5. Conclusions

In the present study we have used numerical thermo-mechanical models to evaluate different hypotheses proposed to explain the origin and evolution of the Canary Islands hotspot, namely edge-driven convection (EDC) and an upper mantle plume upwelling. EDC models predict melt generation only when assuming a relatively high potential temperature and a sharp craton edge. We show that the steeper the craton edge, the more melt volume is generated. Modelled melting occurs in a narrow area adjacent to the craton edge, which is in contradiction with the geographic distribution of the Canary Islands. Moreover, purely EDC models developed in this study are unable to predict the large thermal anomaly beneath the islands inferred in previous studies.

Models where the ascent of an upper mantle plume is induced result in an asymmetric mantle flow pattern and a lateral migration of the plume due to the interplay with a strong lithospheric heterogeneity. The predicted westward migration of the upper asthenosphere thermal anomaly is consistent with the overall westward decrease of the age of the islands. These models provide a plausible explanation for the observed discrepancies between both the direction and rate of volcanic age variation of the Canary Islands and the direction and rate of the Nubia absolute plate motion.

Funding

The present research has been funded by Spanish Ministry of Science and Innovation projects PGC2018-095154-B-I00, PID2020-114854GB-C22 (A.M. Negredo and J. Fullea) and Salvador de Madariaga mobility grant PRX18/00341. J. Rodríguez and J. van Hunen acknowledge funding from the UK Natural and Environmental Research Council, NE/M000281/1. J. Fullea is supported by an Atracción Talento senior fellowship (2018-T1/AMB/11493) funded by Comunidad Autónoma de Madrid (Spain).

CRediT authorship contribution statement

Ana M. Negredo: Conceptualization, Investigation, Methodology, Software, Visualization, Writing – original draft. **Jeroen van Hunen:** Conceptualization, Investigation, Methodology, Writing – review & editing. **Juan Rodríguez-González:** Conceptualization, Methodology, Software, Writing – review & editing. **Javier Fullea:** Conceptualization, Investigation, Writing – review & editing.

Declaration of competing interest

The authors declare that they have no known competing financial interests or personal relationships that could have appeared to influence the work reported in this paper.

Acknowledgements

We are very grateful to the editor, Antonio Manjón-Cabeza Córdoba and an anonymous reviewer for their very constructive reviews. We thank Nicola Celli for providing us with the cross sections of SA2019 tomographic model shown in Fig. 2. Cecilia Albizúa is acknowledged for discussions. We thank the Computational Infrastructure for Geodynamics (geodynamics.org) which is funded by the National Science Foundation under award EAR-0949446 and EAR-1550901 for supporting the development of ASPECT. Juliane Dannberg is kindly acknowledged for her support with ASPECT simulations. Figures were created with ParaView, Gnuplot, GMT and Matlab environments.

Appendix A. Supplementary material

Supplementary material related to this article can be found online at https://doi.org/10.1016/j.epsl.2022.117506.

References

Abdel-Monem, A., Watkins, N.D., Gast, P.W., 1971. Potassium–Argon ages, volcanic stratigraphy, and geomagnetic polarity history of the Canary Islands: Lanzarote, Gran Canaria, and La Gomera. Am. J. Sci. 271, 490–521.

Ancochea, E., Barrera, J., Bellido, F., Benito, R., Brändle, J., Cebriá, J., Coello, J., Cubas, C., De La Nuez, J., Doblas, M., 2004. Canarias y el vulcanismo neógeno peninsular. In: Vera, J.A. (Ed.), Geología de España. SGE-IGME, Madrid, pp. 635–682.

Anguita, F., Hernán, F., 2000. The Canary Islands origin: a unifying model. J. Volcanol. Geotherm. Res. 103, 1–26. https://doi.org/10.1016/S0377-0273(00)00195-5.

Ballmer, M., Ito, G., van Hunen, J., Tackley, P.J., 2011. Spatial and temporal variability in Hawaiian hotspot volcanism induced by small-scale convection. Nature 4, 457–460. https://doi.org/10.1038/ngeo1187.

Balogh, K., Ahijado, A., Casillas, R., Fernandez, C., 1999. Contributions to the chronology of the Basal Complex of Fuerteventura, Canary Islands. J. Volcanol. Geotherm. Res. 90, 81–101. https://doi.org/10.1016/S0377-0273(99)00008-6.

Bangerth, W., Dannberg, J., Gassmoeller, R., Heister, T., 2020. ASPECT: Advanced Solver for Problems in Earth's ConvecTion. User Manual. https://doi.org/10.6084/m9.figshare.4865333.v7.

Bredow, E., Steinberger, B., Gassmöller, R., Dannberg, J., 2017. How plume-ridge interaction shapes the crustal thickness pattern of the Réunion hotspot track. Geochem. Geophys. Geosyst. 18, 2930–2948. https://doi.org/10.1002/2017GC006875.

Carracedo, J.C., Day, S., Guillou, H., Rodríguez Badiola, E., Cañas, J.A., Pérez-Torrado, F.J., 1998. Hotspot volcanism close to a passive continental margin: the Canary Islands. Geol. Mag. 135, 591–604.

Celli, N.L., Lebedev, S., Schaeffer, A.J., Ravenna, M., Gaina, C., 2020. The upper mantle beneath the South Atlantic Ocean, South America and Africa from waveform tomography with massive datasets. Geophys. J. Int. 221, 178–204. https://doi.org/10.1093/gji/ggz574.

Christensen, U., 1984. Convection with pressure- and temperature-dependent non-Newtonian rheology. Geophys. J. R. Astron. Soc. 77, 343–384. https://doi.org/10.1111/j.1365-246X.1984.tb01939.x.

Civiero, C., Strak, V., Custódio, S., Silveira, G., Rawlinson, N., Arroucau, P., Corela, C., 2018. A common deep source for upper-mantle upwellings below the Ibero-western Maghreb region from teleseismic P-wave travel-time tomography. Earth Planet. Sci. Lett. 499, 157–172. https://doi.org/10.1016/j.epsl.2018.07.024.

Courtillot, V., Davaille, A., Besse, J., Stock, J., 2003. Three distinct types of hotspots in the Earth's mantle. Earth Planet. Sci. Lett. 205, 295–308. https://doi.org/10.1016/S0012-821X(02)01048-8.

Currie, C.A., van Wijk, J., 2016. How craton margins are preserved: insights from geodynamic models. J. Geodyn. 100, 144–158. https://doi.org/10.1016/j.jog.2016.03.015.

Dannberg, J., Heister, T., 2016. Compressible magma/mantle dynamics: 3-D, adaptive simulations in ASPECT. Geophys. J. Int. 207, 1343–1366. https://doi.org/10.1093/gji/ggw329.

Ennih, N., Liégeois, J.P., 2008. The boundaries of the West African Craton, with special reference to the basement of the Moroccan metacratonic Anti-Atlas belt. In: Ennih, N., Liégeois, J.-P. (Eds.), The Boundaries of the West African Craton. In: Geol. Soc. Lond. Spec. Pub., vol. 297, pp. 1–17.

Fishwick, S., Bastow, I.D., 2011. Towards a better understanding of African topography: a review of passive-source seismic studies of the African crust and upper mantle. In: van Hinsbergen, D.J.J., Buiter, S., Torsvik, T.H., Gaina, C., Webb, S. (Eds.), Out of Africa: A Synopsis of 3.8 Ga of Earth History. In: Geol. Soc. Lond. Spec. Pub., vol. 357, pp. 343–371.

French, S., Romanowicz, B., 2015. Broad plumes rooted at the base of the Earth's mantle beneath major hotspots. Nature 525, 95–99. https://doi.org/10.1038/nature14876.

Fullea, J., Camacho, A., Negredo, A.M., Fernández, J., 2015. The Canary Islands hot spot: new insights from 3D coupled geophysical-petrological modelling of the lithosphere and uppermost mantle. Earth Planet. Sci. Lett. 409, 71–88. https://doi.org/10.1016/j.epsl.2014.10.038.

Gassmöller, R., Dannberg, J., Bredow, E., Steinberger, B., Torsvik, T.H., 2016. Major influence of plume-ridge interaction, lithosphere thickness variations, and global mantle flow on hotspot volcanism—the example of Tristan. Geochem. Geophys. Geosyst. 17, 1454–1479. https://doi.org/10.1002/2015GC006177.

Geldmacher, J., Hoernle, K., Bogaard, P.v.d., Zankl, G., Garbe-Schönberg, D., 2001. Earlier history of the z70 Ma old Canary hotspot based on the temporal and geochemical evolution of the Selvagen archipelago and neighboring seamounts in the eastern North Atlantic. J. Volcanol. Geotherm. Res. 111, 55–87. https://doi.org/10.1016/S0377-0273(01)00220-7.

Geldmacher, J., Hoernle, K., Bogaard, P.v.d., Duggen, S., Werner, R., 2005. New 40Ar/39Ar age and geochemical data from seamounts in the Canary and Madeira volcanic province: support for the mantle plume hypothesis. Earth Planet. Sci. Lett. 237, 85–101. https://doi.org/10.1016/j.epsl.2005.04.037.

Globig, J., Fernàndez, M., Torne, M., Vergés, J., Robert, A., Faccenna, C., 2016. New insights into the crust and lithospheric mantle structure of Africa from elevation, geoid, and thermal analysis. J. Geophys. Res. 121, 5389–5424. https://doi.org/10.1002/2016JB012972.

Herzberg, C., Asimow, P.D., 2008. Petrology of some oceanic island basalts: PRIMELT2.XLS software for primary magma calculation. Geochem. Geophys. Geosyst. 9, Q09001. https://doi.org/10.1029/2008GC002057.

Hoernle, K., Zhang, Y.-S., Graham, D., 1995. Seismic and geochemical evidence for large-scale mantle upwelling beneath the eastern Atlantic and western and central Europe. Nature 374, 34–39. https://doi.org/10.1038/374034a0.

Kaislaniemi, L., van Hunen, J., 2014. Dynamics of lithospheric thinning and mantle melting by edge-driven convection: application to Moroccan Atlas mountains. Geochem. Geophys. Geosyst. 15, 3175–3189. https://doi.org/10.1002/2014GC005414.

Katsura, T., 1995. Thermal diffusivity of olivine under upper mantle conditions. Geophys. J. Int. 122, 63–69. https://doi.org/10.1111/j.1365-246X.1995.tb03536.x.

Katz, R.F., Spiegelman, M., Langmuir, C.H., 2003. A new parameterization of hydrous mantle melting. Geochem. Geophys. Geosyst. 4 (9), 1073. https://doi.org/10.1029/2002GC000433.

Kim, D.H., So, B.D., 2020. Effects of rheology and mantle temperature structure on edge-driven convection: implications for partial melting and dynamic topography. Phys. Earth Planet. Inter. 303, 106487. https://doi.org/10.1016/j.pepi.2020.106487.

King, S.D., Anderson, D.L., 1995. An alternative mechanism of flood basalt formation. Earth Planet. Sci. Lett. 136 (3–4), 269–279. https://doi.org/10.1016/0012-821X(95)00205-Q.

King, S.D., Anderson, D.L., 1998. Edge-driven convection. Earth Planet. Sci. Lett. 160 (3–4), 289–296. https://doi.org/10.1016/S0012-821X(98)00089-2.

King, S.D., Ritsema, J., 2000. African hot spot volcanism: small-scale convection in the upper mantle beneath cratons. Science 290, 1137–1140. https://doi.org/10.1126/science.290.5494.1137.

Kronbichler, M., Heister, T., Bangerth, W., 2012. High accuracy mantle convection simulation through modern numerical methods. Geophys. J. Int. 191 (1), 12–29. https://doi.org/10.1111/j.1365-246x.2012.05609.x.

Le Bas, M., Rex, D., Stillman, C., 1986. The early magmatic chronology of Fuerteventura, Canary Islands. Geol. Mag. 123, 287–298. https://doi.org/10.1017/S0016756800034762.

Legendre, C., Meier, T., Lebedev, S., Friederich, W., Viereck-Götte, L., 2012. A shear wave velocity model of the European upper mantle from automated inversion of seismic shear and surface waveforms. Geophys. J. Int. 191, 282–304. https://doi.org/10.1111/j.1365-246X.2012.05613.x.

López, C., Blanco, M.J., Abella, R., Brenes, B., Cabrera Rodríguez, V.M., Casas, B., Domínguez Cerdeña, I., Felpeto, A., Fernández de Villalta, M., del Fresno, C., García, O., García-Arias, M.J., García-Cañada, L., Gomis Moreno, A., González-Alonso, E., Guzmán Pérez, J., Iribarren, I., López-Díaz, R., Luengo-Oroz, N., Meletlidis, S., Moreno, M., Moure, D., Pereda de Pablo, J., Rodero, C., Romero, E., Sainz-Maza, S., Sentre Domingo, M.A., Torres, P.A., Trigo, P., Villasante-Marcos, V., 2012. Monitoring the volcanic unrest of El Hierro (Canary Islands) before the onset of the 2011–2012 submarine eruption. Geophys. Res. Lett. 39, LI3303. https://doi.org/10.1029/2012GL051846.

Manjón-Cabeza Córdoba, A., Ballmer, M.D., 2021. The role of edge-driven convection in the generation of volcanism – part 1: a 2D systematic study. Solid Earth 12, 613–632. https://doi.org/10.5194/se-12-613-2021.

Martínez-Arévalo, C., Mancilla, F.D.L., Helffrich, G., Garcia, A., 2013. Seismic evidence of a regional sublithospheric low velocity layer beneath the Canary Islands. Tectonophysics 608, 586–599. https://doi.org/10.1016/j.tecto.2013.08.021.

Miller, M.S., Driscoll, L.J.O., Butcher, A.J., Thomas, C., 2015. Imaging Canary Island hotspot material beneath the lithosphere of Morocco and southern Spain. Earth Planet. Sci. Lett. 431, 186–194. https://doi.org/10.1016/j.epsl.2015.09.026.

Missenard, Y., Cadoux, A., 2012. Can Moroccan Atlas lithospheric thinning and volcanism be induced by Edge-Driven Convection? Terra Nova 24 (1), 27–33. https://doi.org/10.1111/j.1365-3121.2011.01033.x.

Morgan, W.J., 1971. Convection plumes in the lower mantle. Nature 230, 42–43. https://doi.org/10.1038/230042a0.

Oyarzun, R., Doblas, M., López, J., Cebriá, J.M., 1997. Opening of the central Atlantic and asymmetric mantle upwelling phenomena: implications for long-lived magmatism in western North Africa and Europe. Geology 25, 727–730. https://doi.org/10.1130/0091-7613(1997)025<0727:OOTCAA>2.3.CO;2.

Schubert, G., Turcotte, D.L., Olson, P., 2001. Mantle Convection in the Earth and Planets. Cambridge Univ. Press, Cambridge, U.K., 940 pp.

Shahnas, M.H., Pysklywec, R.N., 2004. Anomalous topography in the western Atlantic caused by edge-driven convection. Geophys. Res. Lett. 31, L18611. https://doi.org/10.1029/2004GL020882.

Sleep, N.H., 2007. Edge-modulated stagnant-lid convection and volcanic passive margins. Geochem. Geophys. Geosyst. 8, Q12004. https://doi.org/10.1029/2007GC001672.

Tetley, M.G., Williams, S.E., Gurnis, M., Flament, N., Müller, R.D., 2019. Constraining absolute plate motions since the Triassic. J. Geophys. Res., Solid Earth 124. https://doi.org/10.1029/2019JB017442.

van den Bogaard, P., 2013. The origin of the Canary Island Seamount Province - new ages of old seamounts. Sci. Rep. 3, 2107. https://doi.org/10.1038/srep02107.

Wang, S., Yu, H., Zhang, O., Zhao, Y., 2018. Absolute plate motions relative to deep mantle plumes. Earth Planet. Sci. Lett. 490, 88–99. https://doi.org/10.1016/j.epsl.2018.03.021.